TECHNICAL ARTICLE

The SESAME materials science beamline for XRD applications

M. Abdellatief,[1,a] L. Rebuffi,[2] H. Khosroabadi,[1] M. Najdawi,[1] T. Abu-Hanieh,[1] M. Attal,[1] and G. Paolucci[1,*]
[1]SESAME (Synchrotron-light for Experimental Science and Applications in the Middle East), Allan, Jordan
[2]Elettra-Sincrotrone Trieste S.C.p.A, Trieste, Italy

We present a detailed description of the SESAME Materials Science (MS) beamline for X-ray diffraction (XRD) applications, presently under construction in Allan, Jordan. The beamline is based on components previously installed at the Swiss Light Source, but modifications in the beamline design have been introduced to match the characteristics of the SESAME storage ring. The SESAME MS beamline will accommodate XRD experiments in the energy range between 5 and 25 keV. The beamline ray tracing analysis at 10 keV estimates the flux at the sample to be of the order of 10^{13} (photons s^{-1}), the energy resolution is about 2 eV and the effective beam size at the sample of 300×2800 μm^2. Investigations of microstruture will be possible as the instrumental broadening, resulted from simulating the diffraction pattern for a standard material, is of the order of 0.01° at 15 keV. A wide range of applications will be possible at the beamline, such as powder diffraction studies, single crystals and *in situ* XRD. The commisioning of the beamline is expected to be in the second half of 2017. © 2017 International Centre for Diffraction Data. [doi:10.1017/S0885715617000021]

I. INTRODUCTION

The SESAME synchrotron radiation laboratory (located in Allan, Balqa, Jordan) is a third-generation synchrotron facility. It will be operated at 2.5 GeV and 400 mA (Smith, 2015). The eightfold SESAME storage ring is composed of 16 double-bend achromat cells and 16 dispersive straight sections, 12 of which can be used for insertion devices. The straight sections have two different lengths, 4.4 and 2.4 m. The storage ring is filled with electron beam by the 800 MeV BESSY-I injector that consists of a 20 MeV classical microtron and 800 MeV booster synchrotron. The injector is already in operation (Attal *et al.*, 2016), while the storage ring is still under installation and it is expected to start its commissioning by the end of 2016. The main storage ring parameters (Attal, 2011) are listed in Table I.

X-ray diffraction (XRD) beamlines in most synchrotrons are considered with high priority because of their wide range of applications in diverse fields, such as Materials Science (MS), biology, pharmacology, and cultural heritage. The MS beamline is one of the first four beamlines, to be installed at SESAME, together with IR (infrared), XAFS (X-ray absorption fine structure)/XRF (X-ray fluorescence), and macromlecular crystallography beamlines. The MS beamline is the first insertion device beamline in SESAME and it will be dedicated to XRD experiments and applications. The radiation source is a wiggler consits of array of NdFe:B permanent magnets (Gozzo *et al.*, 2004; Patterson *et al.*, 2005) arranged periodically along 2 m length. The wiggler, front-end, and optical components (Gozzo *et al.*, 2004;

Patterson *et al.*, 2005) are donations from the MS beamline at the Swiss Light Source (SLS). The instrumentation became available when the SLS beamline went through a complete upgrade in 2009 (Willmott *et al.*, 2013).

Although the beamline components were already operated in SLS (Gozzo *et al.*, 2004; Patterson *et al.*, 2005), some modifications to the beamline design have been necessary, because of technical and machine differences between SLS and SESAME. The SESAME MS beamline energy range is 5–25 keV with 5.8 keV critical energy corresponding to a 12 mm magnetic wiggler gap.

The experimental station will be completely new, and will be provided to host the most commonly used XRD sets up for various kind of samples (e.g. powder, bulk, and single crystals). Instrumental angular and time resolutions are the main aspects to select the detection systems. Moreover, it will be possible to vary samples' enviromental conditions (e.g. temperature, pressure, and chemical environment).

In this paper, the major aspects and specifications of the SESAME MS beamline are discussed.

II. BEAMLINE OUTLINE

A. General overview

The beamline consists of three main sections located after the wiggler W61 source: front-end, optics, and experimental stations. The beamline components and their distances from the wiggler source are tabulated in Table II. The front end is entirely located before the storage ring shielding wall. Directly after the storage ring shielding wall, the optics and the experimental stations are located and they are separated by a connection vacuum pipe to transfer the beam. The main beamline major specifications are summarized in Table III and the beamline layout is shown in Figure 1.

---

a)Author to whom correspondence should be addressed. Electronic mail: mahmoud.abdellatief@sesame.org.jo
* On leave from Elettra-Sincrotrone Trieste S.C.p.A, Trieste, Italy.

TABLE I. The SESAME machine parameters.

Parameter	Unit	Value
Energy	GeV	2.5
Circumference	m	133.2
Emittance x, y	nm.rad	26, 0.26
Energy spread (rms)		1.07×10^{-3}
Tunes x, y		7.23, 6.19
Energy loss/turn	keV	603
Target current	mA	400
Zero-current bunch length	Ps	45
Dipole field	T	1.4554
Beam size σ_x/σ_y at source point	μm	825.9/20.8 (LS)
		820.8/14.2 (SS)
		232.3/81.0 (Dipole)
Beam divergence σ'_x/σ'_y at source point	μrad	43.5/12.49 (LS)
		44.0/18.3 (SS)
		266.6/11.5 (Dipole)
Relativistic electron mass to the rest mass ratio γ		4892

B. The MS source and the front end

The MS source is 2 m long wiggler W61 (Patterson *et al.*, 2005) located along the I09 straight section. The main wiggler parameters are summarized in Table IV, while these parameters were used to calculate the beamline flux spectrum as shown in Figure 2. The minimum magnetic gap is 12 mm, which have been decided based on the minimum vacuum chamber height available at SESAME (10 mm) during the first operation period. This magnetic gap will produce reasonably high flux up to 25 keV with about 6000 W of radiation power. Therefore the front-end station will deal with this high power in order to protect the optical components from damage. The wiggler K factor is 7.8 according to Eq. (1) based on the knowledge of the magnetic field strength B_{max} and the wiggler spatial period length λ_w

$$K = 0.934 \ B_{max}\lambda_w. \quad (1)$$

TABLE II. The location of the major beamline components from the wiggler center.

Components	Distance (m)
Front end	
Wiggler W61	0
Fixed mask I	8.13
Fixed mask II	8.52
Photon shutter	8.92
Bremsstrahlung stopper	9.45
Rotating filter (glassy carbon)	10.39
Horizontal slits	10.9
Vertical slits	11.51
Be windows	13.57
Optics	
Fast absorber	14.12
Filters	14.25
Collimating mirror	15.58
Wire beam position monitor BPM	16.68
Double Si crystal Mono	17.55
Bremsstrahlung stopper	18.44
Focusing mirror	20.01
Photon shutter	21.79
Experimental	
Diffractometer (sample location)	33

The critical energy E_c is another important parameter that divides the radiation spectrum in two equal power regions and it depends on the electrons energy and the wiggler magnetic field. Equation (2) was used to calculate the maximum critical energy E_{Cmax} of the radiation spectrum.

$$E_{C\,max} \ [\text{keV}] = 0.665 \times E_e^2 \ [\text{GeV}^2] \times B_{max}[T], \quad (2)$$

Referring to Figure 1, the desired radiation divergence is defined by fixed aperture masks (horizontal and vertical). Their openings were calculated on the basis of the radiation divergence at the minimum desired energy. The vertical divergence angles $\Delta\theta_V$ of the produced wiggler radiation were calculated at selected energies according to Eq. (3) (Kim, 1989; Patterson *et al.*, 2005). Then the horizontal divergence angles δ_H were calculated according to Eq. (4). Figure 3 shows the calculated divergence angles as function of beam energy, and from which 0.23×1.5 m rad^2 were then selected to be accepted by the second fixed mask. These selected apertures cover most of the desired energy range (5–25 keV) and also limits the total power on the following beamline components.

$$\Delta\theta_V[\text{m rad}] = \frac{\sqrt{8\ln 2} \times 1000 \times 0.58}{\gamma} \times \sqrt{\frac{E_c}{E}}, \quad (3)$$

$$\delta_H(E) = K \ \Delta\theta_V(E). \quad (4)$$

While the fixed masks cut a large portion of the photon beam power, the heat load on them is quite high and therefore they must be water-cooled. The first fixed mask cuts about 1.87 kW and the second one cuts further 1.98 kW. Then a rotating glassy graphite filter cup with 1 mm wall thickness (i.e. 2 mm filter thickness in total) absorbs about 1.54 kW and only 0.614 kW is transmitted to the optics, about 10% of total emitted power. Table V summarizes the total power analysis in the front-end station. The filter rotates to distribute the radiation power load on a large surface area and more details concerning the filter can be found elsewhere (Patterson *et al.*, 2005; Heidenreich and Patterson, 2007). Figure 4 shows that the two fixed masks and the rotating filter reduce drastically the photon flux below ~7 keV.

A photon shutter and a gas bremsstrahlung stopper are located directly after the second fixed mask at 8.9 and 9.5 m, respectively. The shutter and the stopper must be connected to the beamline safety system and must be closed in order to access to the optics hutch. Water-cooled horizontal and vertical slits are located at the end of the front end for more control in the beam size whenever needed.

C. The beamline optics and ray tracing

In this section, a brief description for the main optical components and their scope will be shown; much more details concerning the beamline optical components specifications

TABLE III. The major MS beamline parameters.

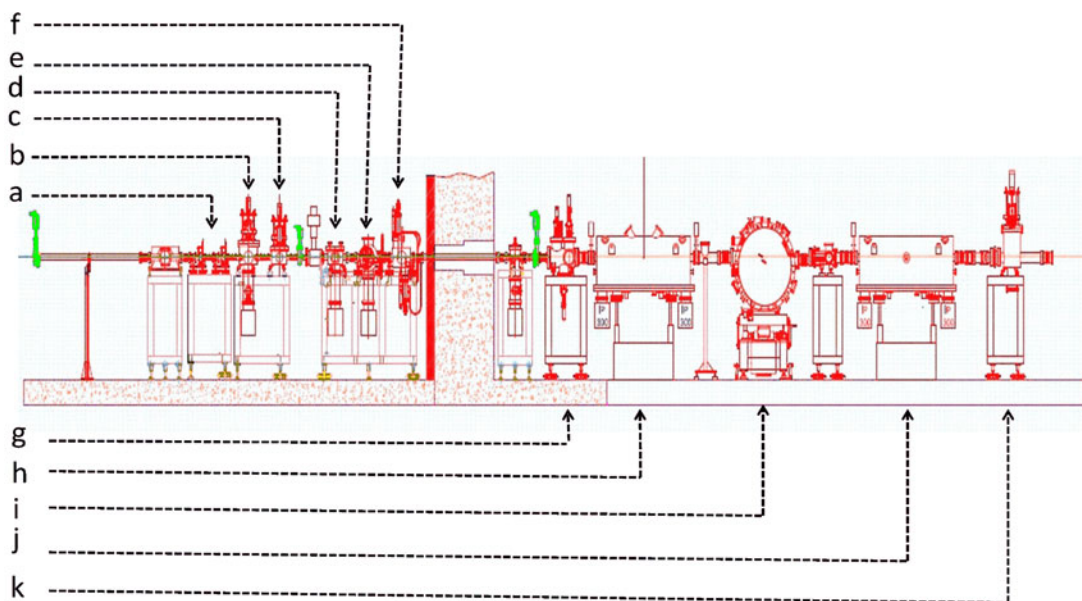| Energy range (keV)	5–25
Accepted divergence (m rad^2)	0.23 (V) $\times$ 1.5 (H)
Flux at the sample at 10 keV (photons s^{-1})	1.6×10^{13}
Energy resolution (eV)	~2
Effective beam size at the sample (FWHM) (μm^2)	300 (v) $\times$ 2800 (h)

Figure 1. (Colour online) Front-end and optics layout starting from left-hand side, fixed masks (a), shutter (b), stopper (c), filter (d), vertical slits (e), horizontal slits (f), fast absorber (g), collimating mirror (h), monochromator (i), focusing mirror (j), and photon shutter (k).

can be found elsewhere (Patterson *et al.*, 2005). Generally, the optical components are aimed at selecting the desired beam energy, focus the beam in horizontal and vertical planes, and to improve the energy resolution. The energy selection is accomplished by a Kozhu double-crystal monochromator in which the first crystal is a water-cooled Si crystal and the second one is a sagittal Si crystal that can be used to focus the beam in the horizontal plane. The beam height decreases at the exit of the monochromator by about 40 mm and in order to keep that height fixed, the second crystal has two perpendicular translational degrees of freedom. The routine operations of the monochromator will be based on Si(111) diffraction planes, while Si(333) diffraction planes will be used to obtain a narrow bandwidth at high energies (>20 KeV).

The monochromator will be preceded by a 1 m length Rh-coated mirror, which will vertically collimate the divergent beam in order to improve the energy resolution. A second mirror similar to first one will be located after the monochromator and will focus the beam in the vertical direction by changing its radius of curvature. The root-mean-square (rms) slope errors of the collimating and focusing mirrors are 3.56 and 2.63 μrad, respectively. Those are the values, which were measured at SLS optics laboratory just before shipping them to SESAME and they are quite different from what is reported for the same mirrors, while they were in operation as SLS (0.75 μrad for the collimating mirror and 1.38 μrad for the

focusing mirror) (Patterson *et al.*, 2005). The choice of rhodium as coating materials limits the energy range to about 25 keV. We simulated the performances of the MS beamline with replacing rhodium with platinum: it was found that this would extend the energy range to 40 keV. This upgrade will be considered at a later stage.

Both mirrors are tilted to grazing angles in order to optimize simultaneously the angular acceptance of the incoming beam and the mirror reflectivity. The grazing angles of the mirrors were selected based on the ray-tracing analysis that will be discussed later in this section. A fast absorber is located at the beginning of the optics hutch and will be connected with the safety system of the beamline to protect the successive optical components whenever necessary. Directly after the fast absorber, two filters are composed of graphite and molybdenum and they are aimed to strip off more power from the white beam when the mirrorless mode is in operation, and so the filters can be used to limit the heat load on the monochromator. For safety, photon and safety shutters are located in the optics hutch to prevent both

TABLE IV. The main parameters of the MS wiggler source.

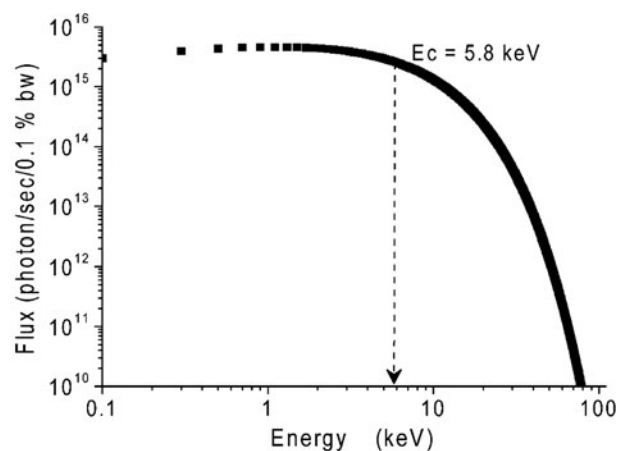|	
Overall W61 length (m)	2
Wiggler gap (mm)	12
Period length λ_w (mm)	60.5
Number of periods	33
Magnetic material	NdFe:B
Pole material	CoFe
Maximum field (T)	1.38
Deviation parameter K	7.8
Critical energy E_c (keV)	5.8
Total power @ 400 mA (kW)	6.01

Figure 2. Flux distribution of the W61 wiggler source at 12 mm magnetic gap.
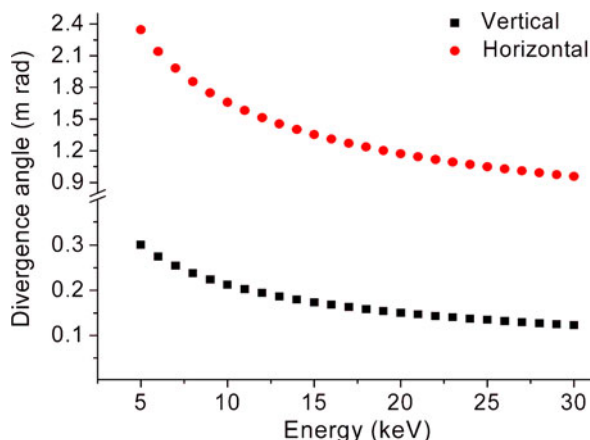
Figure 3. (Colour online) Horizontal and vertical divergences of source radiation at different wiggler gaps.

Figure 4. (Colour online) Flux distribution at the major components in the front end.

synchrotron radiation and gas bremsstrahlung radiation and their control is connected to the beamline safety system to allow access to the experimental hutch. The photon shutter is placed after the second mirror at the end of the optics hutch, while on the other hand the safety shutter is placed immediately after the monochromator.

III. ESTIMATION OF THE FLUX AT SAMPLE VIA RAY TRACING

The flux from the source, integrated in the angular acceptance of the front-end mask (ph/s/0.1%BW) has been calculated with the software SPECTRA (Tanaka and Kitamura, 2001; Tanaka, 2014), using Eq. (5).

$$
\begin{aligned}
flux(E)^{\mathrm{SPECTRA}} &= 0.1\%E \int_{MASK} flux\_density(E')dE' \\
&= flux\_density(E)^{\mathrm{MASK}} \times 0.001 \times E,
\end{aligned}
\tag{5}
$$

where the *flux_density* (E) is the number of photons per second, per unit of area, per unit of solid angle, per unit of energy (eV). In other words, the flux calculated by SPECTRA represents a flux density, integrated into the front-end mask area, and angular acceptance, and then integrated into a bin that is, for every energy value, centered on the energy value E and equal to a bandwidth equal to 0.1% of the energy value.

The real bandwidth *real_BW(E)* of the entire beamline up to the experiment is, in the most general case, depending on energy, then, to obtain the flux in terms of photons s^{-1} at the experiment, the calculation proceed as follows:

$$
\begin{aligned}
real\_flux(E) &= flux\_density(E)^{\mathrm{MASK}} \cdot real\_BW(E) \\
&= flux(E)^{\mathrm{SPECTRA}} \cdot \frac{real\_BW(E)}{0.001 \cdot E}.
\end{aligned}
\tag{6}
$$

TABLE V. Front-end power analysis.

	Power in (kW)	Power out (kW)	Absorbed power (kW)
Fixed mask 1	6	4.13	1.87
Fixed mask 2	4.13	2.15	1.98
Rotating filter	2.15	0.614	1.54

We used SHADOW3, through its last distribution ShadowOui (Rebuffi and Sanchez del Rio, 2016), to calculate the *real_BW* (E), providing an accurate ray-tracing simulation, able to take into account not only geometrical factors, but also physical factors like absorption/scattering of the initial photon beam, reducing its intensity. In other words, taking into account the following properties:

- Absorption coefficient of screens/filters,
- Reflectivity of mirrors/multilayers,
- Diffraction profile of crystals,
- Slope errors of mirrors.

In order to be compliant with the SPECTRA calculations, the rays from the source emitted only within the angular acceptance were considered in the SHADOW simulation.

Then source has been setup with an energy range with central energy the one of interest and with the smallest possible aperture in order to keep high the statistical goodness, but it is big enough to completely contain the energy distribution emerging from the beamline, which is the result of the combined effects of all the optical elements and in particular the monochromator. An inspection of the energy distribution emerging from the double-crystal monochromator shown in Figure 5 shows that the obvious choice is a narrow box around a central value, whose full-width at half-maximum (FWHM) is considered the monochromator bandwidth, but having tails that can extend to values that can be ~5 times the bandwidth value. Thus, if the initial energy range does not contain completely this energy distribution, the calculation of the beamline efficiency will underestimate the final flux.

The efficiency of the beamline is calculated via SHADOW, that produces an initial amount of rays (in our calculations 1 000 000), assigning intensity (square modulus of the electric field) 1 each. At the beginning, the total beam intensity is equal to the number of rays, but during the ray tracing not only an amount of rays become a "lost ray", being geometrically lost by the optical layout, but every "good ray" reduces its intensity trough the different kind of interactions with the elements composing the optical elements (diffraction from crystal, reflection from mirrors, absorption from filters, etc.). The total intensity at the end is the sum of the intensities of the "good rays", and the efficiency of the beamline,
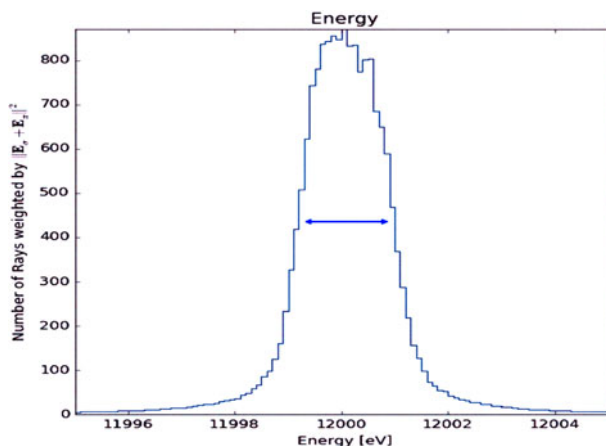
Figure 5. (Colour online) Simulated energy distribution emerging from the double-crystal monochromator at 12 keV. Bandwidth is 1.7 eV, but the tails of the distribution comprehend a ∼10 eV range.

corresponding the chosen energy range, is:

$$\text{Efficiency}(\Delta E_{\text{SOURCE}}) = \frac{I_{\text{SAMPLE}}^{\text{good}}}{I_{\text{SOURCE}}} = \frac{I_{\text{SAMPLE}}^{\text{good}}}{N_{\text{SOURCE}}^{\text{rays}}}. \qquad (7)$$

In order to calculate this efficiency by means of flux of photons available at the sample, the final image plane of the simulation must be chosen in the position of the sample, and by putting in the same position a cutting slit it is possible to take into account also an effective area (i.e. representing the typical sample shape).

The real bandwidth *real_BW(E)* of the entire beamline up to the experiment is finally obtained via SHADOW with the following formula:

$$real\_BW(E) = \Delta E_{\text{SOURCE}} \cdot \text{Efficiency}(\Delta E_{\text{SOURCE}})$$

$$= \Delta E_{\text{SOURCE}} \cdot \frac{I_{\text{SAMPLE}}^{\text{good}}}{N_{\text{SOURCE}}^{\text{rays}}}. \qquad (8)$$

Consequently, the flux at sample is obtained by the following expression:

$$flux\_at\_sample(E) = \text{flux}(E)^{\text{SPECTRA}} \cdot \frac{\Delta E_{\text{SOURCE}}}{0.001 \cdot E}$$

$$\cdot \frac{I_{\text{SAMPLE}}^{\text{good}}}{N_{\text{SOURCE}}^{\text{rays}}}. \qquad (9)$$

This final quantity is expressed in photons s^{-1}. In Figure 6, the simulation results obtained for several energy values are visible. As a note, the Si(111) planes where used for the monochromator in all the simulations, except the final 25 keV one, where Si(333) planes were used.

A. Diffraction station and the instrumental resolution

The experimental station shall be designed to provide high degree of flexibility to host most of the XRD sets up and techniques. A six-circle diffractometer is suitable from many aspects, firstly it is perfect for single-crystal and flat samples and moreover it can be used for powder diffractions in the transmission mode, which is the main priority. A
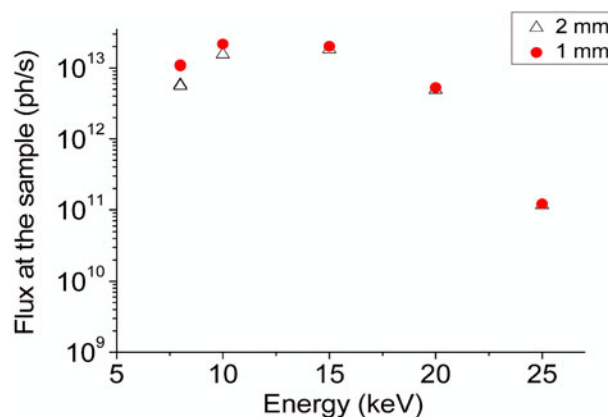

Figure 6. (Colour online) Calculated flux at the sample resulted from the ray tracing considering 1 mm (circles) and 2 mm (triangles) total filter thickness.

capillary spinner, flat plate spinner, liquid nitrogen cryostat, hot air blower, capillary furnace, and flat plate furnace will be considered for the samples enviromental control.

The detector selection is highly based on the experiment requirements, while the time and the instrumental resolutions are the most important parameters for the XRD experiments. For high-resolution XRD needed for microstuctural investigations, a high-energy resolution as well as high-angular resolution are mandatory requirements. Improving the energy resolution could be possible by operating the monochromator at high diffraction planes, but this would reduce the flux at the sample.

On the other hand, the angular resolution can be improved by receiving a relativley collimated and parallel beam at the sample by focusing the beam at the detector location. In addition to that, using a crystal analyzer instead of slits system has a significant influence on the angular resolution. Also the crystal analyzer enhances the diffraction signal-to-background ratio. Although using the analyzer–detecor system would provide high data quality, but it takes a relatively long time for one set of data collection. Using a set of analyzers–detectors would be a good solution to shorten the experimental time. In any case, for time-resolved XRD experiments, the hours time scale which can be achieved by the crytstal analyzers–detectors is quite much and therfore another detection system with a fast read out is highy needed. A linear strip detector (e.g. MYTHEN2 X-DECTRIS Company) is a good compromise and will be a second detection system parallel to the point detecor. The linear strip detector detector is a semiconductor detector, which receives the diffracted X-rays and converts them into electron–hole pairs, which are then separated by an applied voltage. The angular resolution in this case depends on the pixel size of the detector, the distance of the detector from the sample, and finally the sample size according to Eq. (10) (Gozzo et al., 2004).

$$\Delta\theta = 2 \tan^{-1}\left[\frac{(D + P)}{2L}\right], \qquad (10)$$

$\Delta\theta$ is the angular resolution in degree; D is the diameter of the capillary contains the sample; P is the detector pixel size; L is the distance between the detector and the sample.

Based on Eq. (10), the angular resolution is about 0.02 when 0.3 mm capillary is used considering a strip of
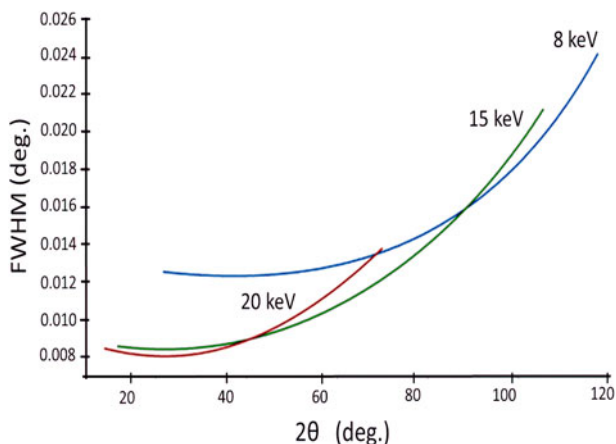
Figure 7. (Colour online) The FWHM of the simulated LaB₆ XRD patterns at selected energies.

MYTHEN detector of 50 μm pixel size when it is located 1 m away from the sample.

The last detection system is the PILATUS 300 K area detector, freely offered by DECTRIS company, and it will be dedicated to *in situ* XRD and single-crystal diffraction. The read-out time of the PILATUS 300 K is of the order of 7 ms and its area is 83.8×106.5 mm². Changing the height of the detector together with controlling the sample to detector distance should be considered to cover a reasonable 2θ range.

From the ray tracing, the simulated diffraction pattern for a standard sample (LaB₆ is considered) at selected energies were obtained, and from which the instrumental broadenings as a function of 2θ are shown in Figure 7, while the produced instrumental broadening is of the order of 0.010, which is quite good for microstructure applications (Rebuffi *et al.*, 2015). Also the simulation results match with the experimental measurements for the instrumental broadening for the same optics used in the simulation at the old SLS MS beamline (Gozzo *et al.*, 2004).

By completing the experimental hutch furnishing, the MS beamline then will provide a wide range of applications, which can be summarized as follows:

- Phase identification,
- Microstructural studies,
- Residual stress and texture studies,
- PDF studies,
- Grazing angle and reflectivity,
- Single-crystal diffraction and structural solution,
- *In situ* XRD and kinetics studies.

IV. CONCLUSION

In this paper, the design analysis for the SESAME MS beamline, in the construction phase, and the changes needed compared the old design for the same components at SLS was discussed. In the initial operation period, the wiggler magnetic gap will be higher (12 mm) compared with its previous operation at SLS (8 mm), but also because of the slightly higher electron beam energy (2.5 instead of 2.4 GeV) it will still produce a reasonably high flux even at high energies. Secondly, it was decided to use a smaller horizontal acceptance (1.5 m rad instead of 2.5 m rad at SLS) in order to limit the incident power on the filter and consequently on

the successive optics components. This is very crucial point because previously the high-power load on the filter caused lots of problems, which led to many changes in the filter bearing connections from metallic to ceramic ones. Then the ray-tracing analysis was applied to simulate the beamline, taking into account most of the physical features of the optics components, to optimize the beamline optics parameters to improve the beam quality at the sample in terms of flux and beam size. The expected flux at the sample resulted from the ray tracing was quite high of the order of 10^{13} photons s^{-1}; which represents the total flux in the effective beam area at the sample location (300×2800 μm²). The instrumental broadening also is very small of the order of 0.01°, which make it possible to study the microstructure for large and nanocrystals. Finally, the plan for the experimental station is to use a six-circle diffractometer and three detections system. Firstly, a crystal analyzer-point detector for high angular resolution needs. Secondly, a linear strip detector for both angular and time-resolution requirements will be considered. The last detector system is the PILATUS 300 K area detector for single-crystal experiments.

Attal, M. (**2011**). *The Reference Optics for SESAME Storage Ring (Report SES-TS-SR-OP)* (SESAME synchrotron, Allan).

Attal, M., Huttel, E., Manukyan, K., Saleh, I., Foudeh, D., Makahleh, F., Shehab, M., Jafar, S., Abid, I., Ismail, A., Hamad, A., Abu Hanieh, Th., Mansouri, M., Al Mohammad, H., Sawai, N., and Al-Najdawi, M. (**2016**). *Commissioning of SESAME Booster* (IPAC16, Busan, South Korea), p. 2880–2882.

Gozzo, F., Schmitt, B., Bortolamedi, Th., Giannini, C., Guagliardi, A., Lange, M., Meister, D., Maden, D., Willmott, P., and Patterson, B. D. (**2004**). "First experiments at the Swiss Light Source Materials Science beamline powder diffractometer," J. Alloys Compd. **362**, 206.

Heidenreich, G. and Patterson, B. D. (**2007**). "A rotating filter for the wiggler beamline at the Swiss Light Source," Nucl. Instrum. Methods Phys. Res. A **577**, 751.

Kim, K. J. (**1989**). "Physics of Particle Accelerators," in *Characteristics of Synchrotron Radiation*, edited by M. Month and M. Dienes (AIP Conf. Proc., New York), Vol. 184, pp. 565–632.

Patterson, B. D., Abela, R., Auderset, H., Chen, Q., Fauth, F., Gozzo, F., Ingold, G., Kühne, H., Lange, M., Maden, D., Meister, D., Pattison, P., Schmidt, Th., Schmitt, B., Schulze-Briese, C., Shi, M., Stampanoni, M., and Willmott, P. R. (**2005**). "The materials science beamline at the Swiss Light Source: design and realization," Nucl. Instrum. Methods Phys. Res. A **540**, 42.

Rebuffi, L. and Sanchez del Rio, M. (**2016**). "ShadowOui: a new visual environment for X-ray optics and synchrotron beamline simulations," J. Synchrotron Radiat. **23**, 1357.

Rebuffi, L., Scardi, P., and del Rio, M. S. (**2015**). "Design and management of a powder diffraction beamline for Line Profile Analysis: a realistic ray-tracing approach," Powder Diffr. **30**, 56.

Smith, C. L. (**2015**). "SESAME for science and peace," Nat. Photonics **9**, 550.

Tanaka, T. (**2014**). "Numerical methods for characterization of synchrotron radiation based on the Wigner function method," Phys. Rev. Accel. Beams **17**, 060702.

Tanaka, T. and Kitamura, H. (**2001**). "SPECTRA: a synchrotron radiation calculation code," J. Synchrotron Radiat. **8**, 1221.

Willmott, P. R., Meister, D., Leake, S. J., Lange, M., Bergamaschi, A., BÖge, M., Calvi, M., Cancellieri, C., Casati, N., Cervellino, A., Chen, Q., David, C., Flechsig, U., Gozzo, F., Henrich, B., Jäggi-Spielmann, S., Jakob, B., Kalichava, I., Karvinen, P., Krempasky, J., Lüdeke, A., Lüscher, R., Maag, S., Quitmann, C., Reinle-Schmitt, M. L., Schmidt, T., Schmitt, B., Streun, A., Vartiainen, I., Vitins, M., Wang, X., and Wullschleger, R. (**2013**). "The Materials Science bamline upgrade at the Swiss Light Source," J. Synchrotron Radiat. **20**, 667.